Effects of minor B addition on microstructure and properties of $Al_{19}Co_{20}Fe_{20}Ni_{41}$ eutectic high-entropy alloy

Jun-jie FENG[1], Shuo GAO[1], Kun HAN[1], Yi-dong MIAO[1], Ji-qiu QI[1], Fu-xiang WEI[1],
Yao-jian REN[1], Zhen-zhen ZHAN[1], Yan-wei SUI[1], Zhi SUN[1], Peng CAO[2]

1. Jiangsu Province Engineering Laboratory of High Efficient Energy Storage Technology and Equipments,
School of Materials and Physics, China University of Mining and Technology, Xuzhou 221116, China;
2. Department of Chemical and Materials Engineering, The University of Auckland,
Private Bag 92019, Auckland, 1142, New Zealand

Abstract: The simultaneous strengthening of mechanical and magnetic properties is an ideal fabrication strategy for soft-magnetic materials. A non-equiatomic $Al_{19}Co_{20}Fe_{20}Ni_{41}$ eutectic high-entropy alloy was prepared to investigate the alloying effect of B on the microstructure evolution, phase formation, mechanical and soft-magnetic properties. With the increase in B content, the microstructures of $(Al_{19}Co_{20}Fe_{20}Ni_{41})_{100-x}B_x$ alloys transformed from the initial lamellar eutectic structure (x=0) to the divorced eutectic structure (x>0.6). Fine borides precipitated in the intergranular phase (x≥0.6). The hardness of alloys increased from HV 328.66 to HV 436.34 and the compression mechanical performance displayed a transition from plastic material to brittle material. The $Al_{19}Co_{20}Fe_{20}Ni_{41}$ alloy possesses good soft-magnetic properties, and the minor B addition has little effect on it. Increasing the resistivity can effectively reduce the eddy current loss when used as a soft-magnetic material.

Key words: high-entropy alloy; B element; microstructure; mechanical properties; soft-magnetic properties

1 Introduction

In 2004, a new concept of high-entropy alloys (HEAs) which consist of four or more principal elements in equimolar or near-equimolar compositions was proposed by CANTOR et al [1] and HSU et al [2]. The unique composition design gives the high-entropy alloys excellent hardness, strength, wear resistance, corrosion resistance and irradiation resistance [3−7], etc. The novel concept and outstanding performance of the high-entropy alloys have aroused the interest of many scholars around the world [4,8].

The good casting performance of eutectic high-entropy alloys (EHEAs) overcomes the defects of most traditional high-entropy alloys in actual application, such as insufficient strength and excessive brittleness. Some EHEAs even exhibit extremely high strength, superior thermal stability and high ductility. Numerous researches based on the eutectic high-entropy alloys have been done. For example, $AlCoCrFeNi_{2.1}$ EHEAs with ordered FCC($L1_2$) and ordered BCC($B2$) two-phase lamellar structure display good mechanical property at both room and elevated temperatures up to 700 °C [9,10]. By adding Al element, the ductile face-centered cubic (FCC) was substituted by the hard body-centered cubic phase (BCC) which brought about excellent wear property for $Al_xCrCuFeNi_2$ EHEAs [11]. $CoCrFeNiNb_x$ EHEAs composed of a ductile FCC phase and a hard Laves phase with fine

laminar structures display an excellent comprehensive mechanical performance [12]. Al_xCrFeNi EHEAs composed of the disordered [Cr, Fe] solid solution and ordered NiAl intermetallic display an excellent mechanical property along with a good combination of compressive strength and plastic deformation, which is due to the strengthening effect of precipitated nanoparticles through amplitude modulation decomposition [13]. Based on the mixing enthalpy, $(AlTa_{0.76})_x$CoCrFeNi$_{2.1}$ alloys consisting of soft FCC, hard $B2$ and the Laves phases were designed and investigated [14]. Furthermore, adding aluminum can effectively adjust the ratio of FCC to BCC phase in Fe−Co−Ni-based HEA to achieve a combination of excellent magnetic properties, high strength and sufficient stability [15]. Above all, tailoring the chemical composition and atomic mixing enthalpy is a sensible way to adjust the content of two-phase and the composition of precipitation phase in order to design high performance EHEAs [16,17].

From the perspective of atomic structure, the traditional solution strengthening theory holds that the distortion caused by atoms of the substitutional solid solution in the matrix lattice is spherical symmetry, and the addition of interstitial atoms will cause asymmetric lattice distortion [18]. Therefore, the addition of a few interstitial atoms in the alloy can play a significant solution strengthening effect, and the strength and toughness are higher than interstitial solution strengthening [19]. By adding new elements that have tremendous differences in low negative mixing enthalpies and atomic radius with original element of alloy [20,21], for instance, B element, is a wise strategy to enhance the wear resistance and compression strength [22,23]. The microstructure and morphology of the alloy were effectively regulated, and the mechanical properties were enhanced through adding B atoms with small atomic radius and excellent diffusion performance by the phase transition process [2,24]. Eutectic high-entropy alloys have higher lattice distortion than conventional alloys. In addition, the types and sizes of polyhedral gaps in FCC phase and BCC phase structures are different. The high-entropy effect can inevitably affect the solid solution of B atoms and the precipitation of borides. It is a prospective strategy to optimize the mechanical properties and soft-magnetic properties through

regulating the alloying minor elements and the size of grain [25]. Until now, studies on adding minor B element to EHEAs as an excellent modified element is still limited.

In this work, the effect of minor B element addition on the microstructure evolution and performance for the $(Al_{19}Co_{20}Fe_{20}Ni_{41})_{100-x}B_x$ alloys was systematically investigated in the range of 0 to 2% in molar fraction. It was expected to illustrate the solid solution strengthening mechanism of B atoms and precipitation rule of boride phase, explore the functional fields on the characteristics of miniaturization and high value-added in EHEAs, and promote the industrial application of eutectic high-entropy alloys.

2 Experimental

The $(Al_{19}Co_{20}Fe_{20}Ni_{41})_{100-x}B_x$ (mole fraction x=0, 0.3, 0.6, 1.0 and 2.0, denoted as B_0, $B_{0.3}$, $B_{0.6}$, $B_{1.0}$ and $B_{2.0}$, respectively) alloys were prepared by vacuum arc furnace under a high purity Ar atmosphere using pure elements of Al, Co, Ni, Fe and B (99.9 wt.%). Approximately 50 g button ingots were flipped and remelted seven times to improve the homogeneity of alloys, and then directly solidified in copper mould with water cooling. Ultrasonic cleaning, inlaying and polishing carried out after the ingots were cut by linear cutting technology into different sizes.

X-ray diffraction instrument (XRD, Bruker D8, Cu K$_a$) was used to analyze the phase constitution at a scanning rate of 8 (°)/min. The microstructure and phase composition of alloy were examined using a scanning electron microscope (SEM, FEI Quanta TM 250) equipped with energy dispersive spectrometry (EDS). Sample size for compression mechanical performance test was d5 mm × 10 mm. RT compressive tests were conducted at a compression rate of 1 mm/min. Hardness measurements were carried out using the Vickers hardness tester (HV−5) under a load of 1 kg for 15 s. The precise resistance tester (JK2516) was used to measure and calculate the electrical resistance of samples according to ASTM B193−02(2014). The magnetization curves were measured by the vibrating sample magnetometer (JDM−13T). Each sample was measured 7 times to obtain the average experimental data.

3 Results and discussion

3.1 Phase identification and microstructure

Figure 1 shows the XRD patterns of $(Al_{19}Co_{20}Fe_{20}Ni_{41})_{100-x}B_x$ alloys. When $x=0$, the alloy exhibits the mixing structures of FCC and BCC, which is consistent with previous research results [26]. The difference in the intensity of the diffraction peaks indicated that preferred orientation may exist in the crystal structure. Besides, the significant decreasing in the intensity of phase diffraction peaks indicated that the lattice structures of FCC and BCC were seriously distorted due to the addition of B atoms. A conclusion can be inferred that the crystal phase structure of alloys has changed with the addition of B atoms.
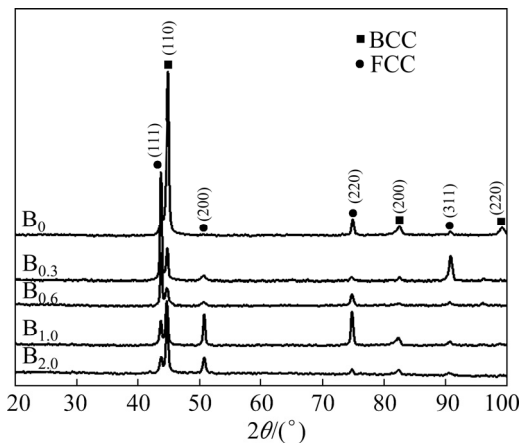

Fig. 1 XRD patterns of $(Al_{19}Co_{20}Fe_{20}Ni_{41})_{100-x}B_x$ alloys

From Fig. 2, it obviously manifests that $(110)_{BCC}$ peak position firstly moves to lower diffraction angle ($x\leq1.0$) and then to higher 2θ angle ($x>1.0$) with the increase of B content. However, the change of $(111)_{FCC}$ peak position shows randomness.

The microstructures of the $(Al_{19}Co_{20}Fe_{20}Ni_{41})_{100-x}B_x$ alloys are shown in Fig. 3. The $Al_{19}Co_{20}Fe_{20}Ni_{41}$ EHEA shows a full eutectic cell morphology. The eutectic cell consisted of a flat structure surrounded by BCC and FCC two-phase layered structure, which had been verified [26]. Based on the SEM−EDS measurements, the dark-colored region is BCC phase enriched with Al and Ni elements, while the light-colored region is FCC phase enriched with Fe and Co elements. The microstructures of $(Al_{19}Co_{20}Fe_{20}Ni_{41})_{100-x}B_x$ alloys are sensitive to the alloy composition. From

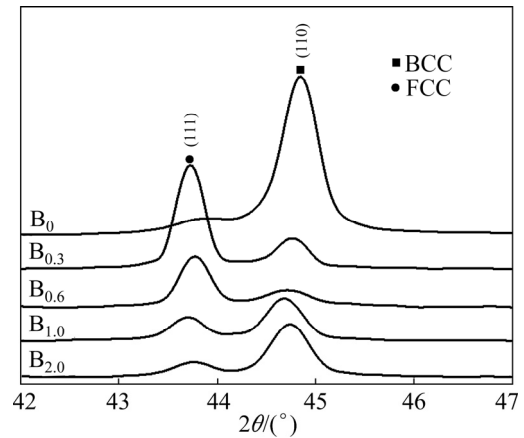**Fig. 2** Enlarged image of $(111)_{FCC}$ and $(110)_{BCC}$ peak

Figs. 3(a−e), the volume fractions of BCC phase in each component alloys are 44%, 51%, 50%, 50% and 53%, respectively. Although the volume fractions of BCC phase and FCC phase change little, the microstructure of alloys transformed from the initial lamellar eutectic structure ($x=0$) to the divorced eutectic structure ($x>0.6$), which was manifested as the disappearance of fine eutectic phase, grain coarsening and significant decrease in grain boundary density. However, the phase compositions of alloys were still a near-eutectic structure. The maximum grain size and obvious FCC phase boundary are shown in Fig. 3(e). In Fig. 3(f), the unique structure of the typical Halo phase was observed and plenty of fine black particles were discovered in the intergranular phase. The grain of BCC phase is significantly coarsened as B content increases, for example, the grain size of Sample $B_{0.3}$ is 0−10 μm, Sample $B_{1.0}$ 10−20 μm, and Sample $B_{2.0}$ 20−50 μm. On account of solidifying in copper mould with water cooling, obvious preferred orientation inevitably existed in the grain of $Al_{19}Co_{20}Fe_{20}Ni_{41}$ alloy and this trend gradually disappeared with the addition of B atoms.

Figure 4 displays the BSE and SE images of $(Al_{19}Co_{20}Fe_{20}Ni_{41})_{100-x}B_x$ alloys. The dark area and bright area were denoted as BCC phase and FCC_1 phase, respectively, while the intergranular phase with light color was represented as FCC_2 phase. When x exceeds 0.6, the existence of FCC_2 phase becomes obvious. Fine black particles were found in FCC_2 phase of Fig. 4(b, d), which were the small hole observed on the surface of the intergranular phase in Fig. 4(a). SEM and EDS results (see Fig. 5 and Table 1) illustrated that the B
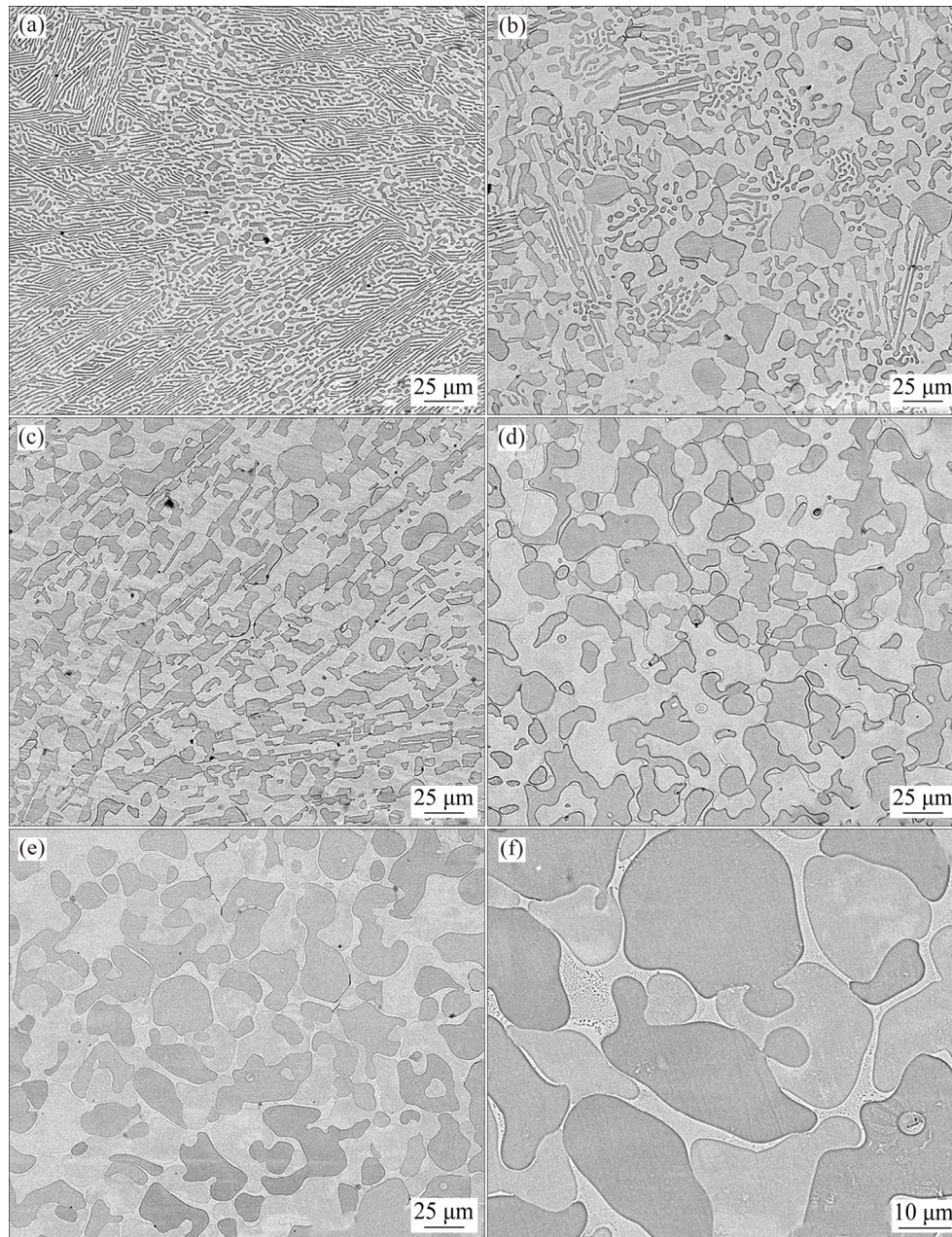
Fig. 3 Microstructures of $(Al_{19}Co_{20}Fe_{20}Ni_{41})_{100-x}B_x$ alloys: (a) $x=0$; (b) $x=0.3$; (c) $x=0.6$; (d) $x=1.0$; (e, f) $x=2.0$

element was only detected in the FCC_2 phase, according to the previous studies, these precipitates are probably fine borides of M_2B [27]. The presence of FCC_2 phase and borides became obvious as B content increased. The grain of BCC phase wrapped by FCC phase and FCC phases wrapped by BCC phase is observed in Figs. 4(b, d). This unique structure is the Halo phase mentioned above. The distribution of each element in two-phase was generally uniform, while the Al element was more concentrated in BCC phase. With the increase of B content, the distribution difference of Al element in BCC and FCC phases decreased.

The intergranular phase was formed by the residual liquid before solidification, whose shape resembled a long and narrow curve extending from the grain boundary. As x exceeds 1.0, the intergranular phase becomes obvious. BCC phase has completely solidified when the intergranular phase begins to solidify. Hence, the contraction of the intergranular phase was hindered by BCC phase, which resulted in the casting thermal stress. BCC phase was subjected to compressive stress while the intergranular phase was subjected to tensile stress. Therefore, the crystalline interplanar spacing of BCC phase decreased. Due to the increase
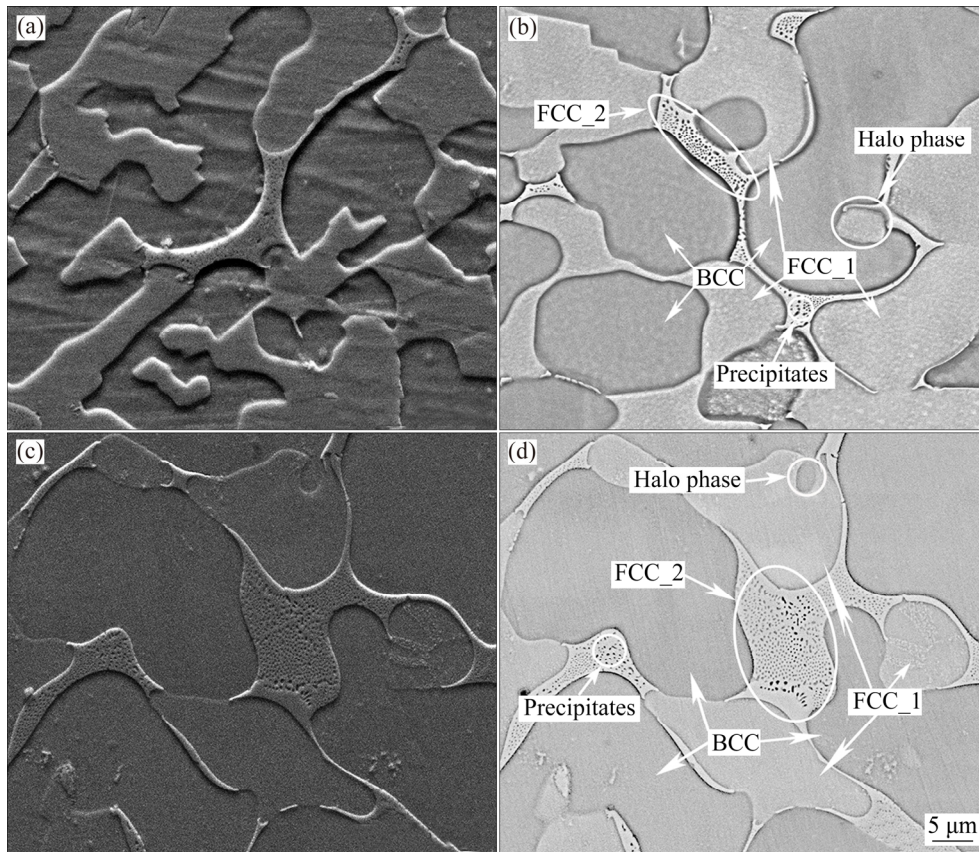
Fig. 4 SEM images of $(Al_{19}Co_{20}Fe_{20}Ni_{41})_{100-x}B_x$ alloys: (a) x=0.6, SE; (b) x=1.0, BSE; (c) x=2.0, SE; (d) x=2.0, BSE
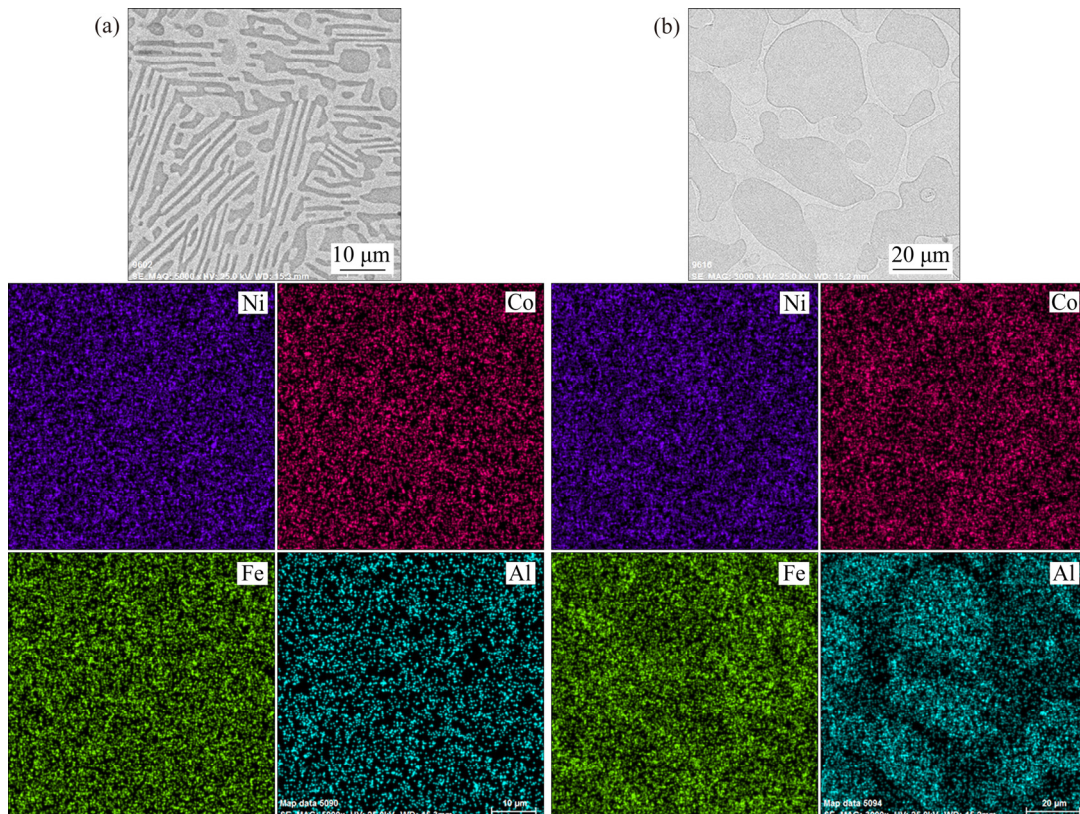

Fig. 5 SEM images and elemental mapping of Ni, Co, Fe and Al for $(Al_{19}Co_{20}Fe_{20}Ni_{41})_{100-x}B_x$ alloys: (a) x=0; (b) x=2.0

Table 1 Chemical compositions of $(Al_{19}Co_{20}Fe_{20}Ni_{41})_{100-x}B_x$ alloys by EDS analysis (at.%)

Alloy	Phase	Al	Fe	Co	Ni	B
B_0	Normal	19.00	20.00	20.00	41.00	0
	BCC	28.67	16.72	17.09	37.52	0
	FCC	14.56	23.97	23.59	37.88	0
$B_{0.3}$	Normal	18.94	19.94	19.94	40.88	0.30
	BCC	29.20	18.10	17.55	35.15	0
	FCC	14.41	23.51	22.98	39.10	0
$B_{0.6}$	Normal	18.89	19.88	19.88	40.75	0.60
	BCC	28.95	16.52	17.18	37.35	0
	FCC_1	15.40	22.82	23.19	38.59	0
	FCC_2	17.78	10.12	9.89	26.63	35.58
$B_{1.0}$	Normal	18.81	19.80	19.80	40.59	1.00
	BCC	23.09	14.83	17.21	44.87	0
	FCC_1	16.20	26.10	22.61	35.09	0
	FCC_2	4.58	16.67	17.77	22.39	38.59
$B_{2.0}$	Normal	18.62	19.60	19.60	40.18	2.00
	BCC	28.59	16.98	17.76	36.67	0
	FCC_1	18.32	26.83	22.01	32.84	0
	FCC_2	2.77	10.59	9.78	12.42	64.44

in volume fraction of the intergranular phase, the $(110)_{BCC}$ peak position ($x>1.0$) shifts toward the high 2θ angle, and then the $(110)_{BCC}$ peak shifts toward low 2θ angle ($x\leq1.0$) on account of lattice distortion.

According to the low negative mixing enthalpy between Al and Ni (−22 kJ/mol), BCC phase (rich in Al and Ni elements) as the primary precipitated phase takes the lead in the nucleation and growth when B element is not added, and the content of Al in the corresponding region decreases with the growth of BCC phase. Thus, the element enrichment area of FCC phase is formed and promotes the growth of FCC phase. As FCC phase grows, Al element will be enriched again and encourages the growth of BCC phase. The lamellar eutectic structure with fine grain is finally obtained by alternating nucleation and synergistic growth of two-phase structures.

However, the enormous differences of atomic size between B element and constituent elements of alloys result in the enrichment of B element in the residual liquid phase before solidification. In addition, compared with solid metal with a long-range ordered lattice, liquid metal without a complete crystal structure can hold more B atoms. The free energy difference between the B atoms in solid alloy and liquid alloy makes it difficult for B atoms to enter the solid phase from the liquid phase during the grain growth process, and it is easy to enter the liquid phase from the solid phase. Therefore, the lattice distortion caused by the addition of B atoms makes the B atoms enriched in the liquid alloy during the solid−liquid coexistence state.

With the growth of BCC phase, a region rich in B element and poor in Al element was formed at the phase boundary of alloy. Although poor Al content was beneficial to forming FCC phase, the enrichment of B element made it difficult for FCC phase to nucleate on the surface of BCC phase. Therefore, enrichment of B element hinders the synergistic growth mechanism of the eutectic structure, and the grain coarsening is attributed to the decrease of nucleation ability. The existence of the Halo phase indicated that the solidification structure of alloys transformed from lamellar eutectic structure to divorced eutectic structure with the increase of B content. When the B content in the intergranular phase was oversaturated and exceeded the solid solution limit of the FCC lattice, as the temperature decreased, supersaturated B atoms precipitated from the intergranular phase (FCC_2 phase) as boride.

3.2 Mechanical properties

The linear graph of Vickers hardness for $(Al_{19}Co_{20}Fe_{20}Ni_{41})_{100-x}B_x$ alloys is shown in Fig. 6. With the increase of B content, the hardness increases from HV 328.66 to HV 436.34. The change of hardness approximately presents a linear rule: $Y_{HV}=56.3x+94.3$, where Y_{HV} is the Vickers hardness. As x increases from 0 to 0.3, changes in volume fraction of two-phase along with the interstitial solid solution strengthening of B atoms offset the effect of phase structure changes (significant grain boundary density decreases and coarsening of grains) on the hardness of the alloy. Therefore, hardness of $B_{0.3}$ alloy increased slightly. As x increases to 0.6, significant increase in hardness is attributed to the combined effect of B atoms solid solution strengthening and borides precipitation strengthening. When x exceeds 0.6,

the quantity of borides precipitates increases linearly with the increase of B content, and the hardness change basically follows the above linear rule. According to the above analysis, the solid solution strengthening effect of B atoms is better than the precipitation strengthening.
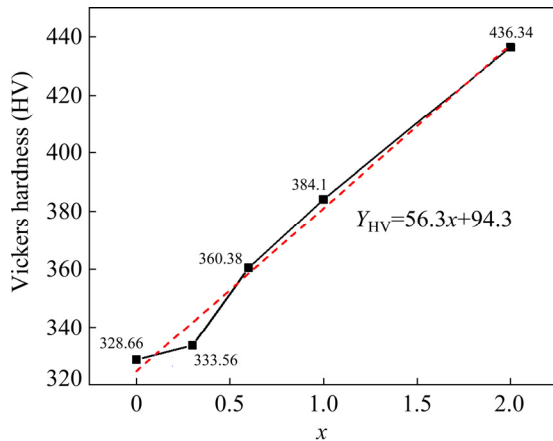

Fig. 6 Linear graphs of Vickers hardness for $(Al_{19}Co_{20}Fe_{20}Ni_{41})_{100-x}B_x$ alloys

Figure 7 shows the compressive stress−strain curves of $(Al_{19}Co_{20}Fe_{20}Ni_{41})_{100-x}B_x$ alloys at a compression rate of 1 mm/min, and the compressive test results are listed in Table 2. The deformation process consists of an elastic deformation stage and a plastic deformation stage, and there is no obvious yield stage. As the B content increases, the yield strength first increases, then decreases, and then increases, while the compression ratio of alloys first increases and then decreases.

The unique cooperative growth mechanism of eutectic structure makes B_0 alloy have high grain
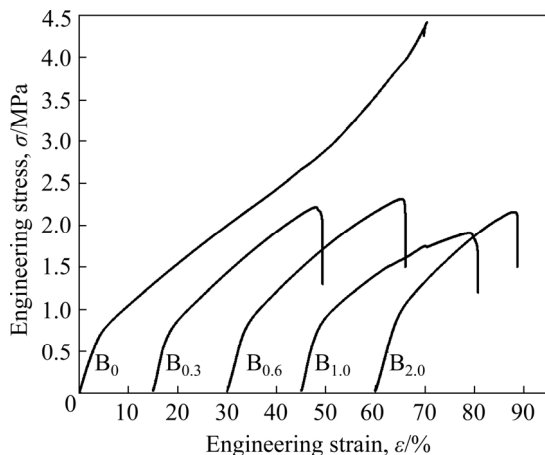

Fig. 7 Compressive engineering stress–strain curves of $(Al_{19}Co_{20}Fe_{20}Ni_{41})_{100-x}B_x$ alloys

Table 2 Compressive mechanical properties of $(Al_{19}Co_{20}Fe_{20}Ni_{41})_{100-x}B_x$ alloys

Alloy	Yield strength/MPa	Compression strength/MPa	Compression ratio/%
B_0	652.7	No fracture	No fracture
$B_{0.3}$	603.2	2213.0	33
$B_{0.6}$	722.1	2312.4	35
$B_{1.0}$	610.5	1902.7	34
$B_{2.0}$	813.0	2060.0	28

boundary density and fine grain size, and thus it possesses the best plasticity. The high phase volume fraction of BCC phase makes B_0 alloy have good yield strength. With the increase of B content, the volume fraction of BCC phase also increases. The lamellar growth mode of eutectic alloys is close to equilibrium in thermodynamics, which can relieve the microscopic stress caused by rapid cooling. However, the addition of B atoms will increase the casting stress during the solidification process, causing the solidification process to gradually deviate from the thermodynamic equilibrium. The decrease in the yield strength of $B_{0.3}$ alloy shows a transition from plastic material properties to brittle material properties, which is actually a manifestation of high stress concentration. This transition comes from the ability of grain boundaries to prevent dislocation diffusion and reduce dislocation accumulation. It is worth noting that the precipitous drop in the yield strength of the $B_{1.0}$ alloy is abnormal. It is the preferred grain orientation that leads to the anisotropic mechanical properties of the $B_{1.0}$ alloy, which is due to the solidification in copper mould with water cooling. Therefore, there is some randomness in the test results. The best yield strength (813 MPa) of $B_{2.0}$ alloy may be due to its high BCC phase volume fraction. In addition, the solid solution strengthening of B atoms and the precipitation strengthening of borides are also reasons for the increase in the yield strength.

Above all, under the combined effects of the decrease in grain boundary density, grain coarsening, solid solution strengthening and precipitation strengthening, the yield strength shows a tendency to first decrease and then increase. $B_{2.0}$ alloy has an excellent compressive plasticity.

3.3 Electrical resistivity and magnetic properties

Figure 8 presents the linear graph of electrical resistivity for $(Al_{19}Co_{20}Fe_{20}Ni_{41})_{100-x}B_x$ alloys. As B content increases, the electrical resistivity increases from 0.875 to 0.936 $\mu\Omega\cdot m$. The change of electrical resistivity is approximately in line with the linear rule: $Y_R=0.0304x+0.0878$, where Y_R is the electrical resistivity.
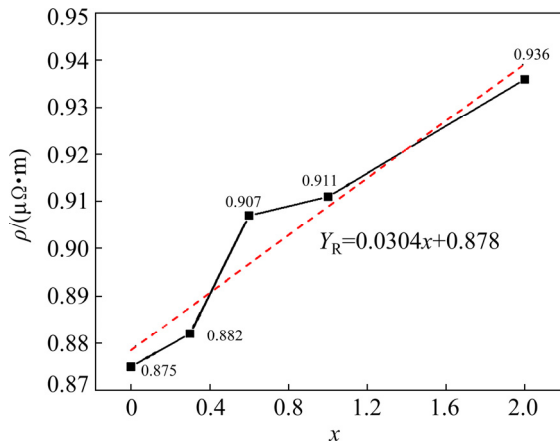

Fig. 8 Linear graph of electrical resistivity for $(Al_{19}Co_{20}Fe_{20}Ni_{41})_{100-x}B_x$ alloys

As x increases from 0 to 0.3, the change of alloy resistivity is the combined effect of the reduction of grain boundaries and lattice distortion. When x increases to 0.6, the increase of lattice distortion and boride precipitation phase greatly change the electrical resistivity, which is similar to the change in microhardness. After that, the increase of the resistivity basically conforms to the linear rule. In summary, electrical resistivity of $Al_{19}Co_{20}Fe_{20}Ni_{41}$ alloy is sensitivity to lattice distortion caused by the addition of B atoms.

The magnetization curves of $(Al_{19}Co_{20}Fe_{20}Ni_{41})_{100-x}B_x$ alloys are shown in Fig. 9, and the magnetization test results are listed in Table 3. The narrow hysteresis loops of $(Al_{19}Co_{20}Fe_{20}Ni_{41})_{100-x}B_x$ alloys conform to the characteristics of soft-magnetic materials. Saturation magnetization (M_s) is mainly determined by the phase composition and atomic-level crystal structure, and is not sensitive to grain size and morphology. There is no obvious regularity between the changes in microstructure and the soft-magnetic properties. Notably, high M_s and low coercivity (H_c) value lead to excellent soft-magnetic performance. As the B content increases, H_c and remanence magnetization (M_r) almost do not change. Due to the non-metallic

nature of element B, the M_s of the alloy decreases. When the resistivity is not considered, the addition of B atoms is not a sensible manufacturing strategy to regulate the soft-magnetic performance of $Al_{19}Co_{20}Fe_{20}Ni_{41}$ alloy.
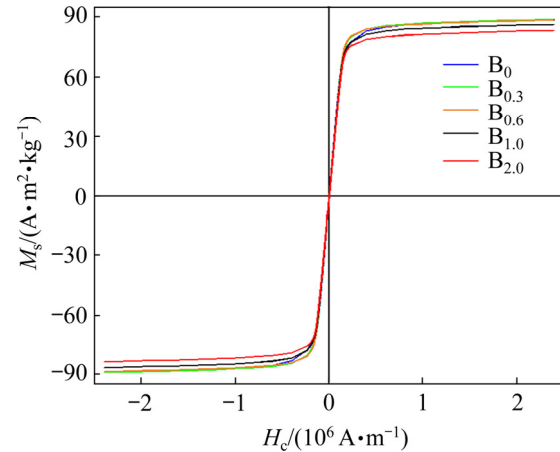

Fig. 9 Magnetization curves of $(Al_{19}Co_{20}Fe_{20}Ni_{41})_{100-x}B_x$ alloys

Table 3 Soft-magnetic properties of $(Al_{19}Co_{20}Fe_{20}Ni_{41})_{100-x}B_x$ alloys

Alloy	$M_s/(A\cdot m^2\cdot kg^{-1})$	$H_c/(A\cdot m^{-1})$	$M_r/(A\cdot m^2\cdot kg^{-1})$
B_0	88.94	2439.85	1.33
$B_{0.3}$	89.16	2411.20	1.30
$B_{0.6}$	88.65	2405.63	1.27
$B_{1.0}$	86.67	2454.17	1.32
$B_{2.0}$	83.71	2431.09	1.29

It is noteworthy that eddy currents formed inside the material may cause loss when soft-magnetic materials are applied in practice. However, the loss caused by vortex will decrease along with the increase of the resistivity. By adjusting the content of B atoms added, the resistivity of the alloy can be effectively increased while avoiding the loss of soft-magnetic properties. According to the above analysis, element B plays a positive role in the application of alloys as soft-magnetic material.

4 Conclusions

(1) $(Al_{19}Co_{20}Fe_{20}Ni_{41})_{100-x}B_x$ alloys display a mixed structure of FCC phase and BCC phase, and the microstructure is sensitive to alloy composition. Fine borides are precipitated in the intergranular phase ($x\geq0.6$). The addition of B atoms facilitates

the microstructure changing from the lamellar eutectic structure (x=0) to the divorced eutectic structure (x>0.6), accompanied with obvious coarsening.

(2) The properties of alloy change from plastic material to brittle material with the increase of B content. Hardness increases from HV 328.66 to HV 436.34, while the yield strength first decreases and then increases (x≥0.3). Mechanical property optimization benefits from the combined action of the decrease in grain boundary density, solid solution strengthening and precipitation strengthening.

(3) The $Al_{19}Co_{20}Fe_{20}Ni_{41}$ alloy possesses good soft-magnetic properties while minor B addition has little effect on it. As B content increases, electrical resistivity increases from 0.875 to 0.936 μΩ·m. When used as soft-magnetic material, the increase in alloy resistivity can effectively reduce the eddy current loss.

Acknowledgments

References

[1] CANTOR B, CHANG I T H, KNIGHT P, VINCENT A J B. Microstructural development in equiatomic multicomponent alloys [J]. Materials Science and Engineering A, 2004, 375: 213−218. https://doi.org/10.1016/j.msea.2003.10.257.

[2] HSU C Y, YEH J W, CHEN S K, SHUN T T. Wear resistance and high-temperature compression strength of FCC $CuCoNiCrAl_{0.5}Fe$ alloy with boron addition [J]. Metallurgical and Materials Transactions A, 2004, 35(5): 1465−1469. https://doi.org/10.1007/s11661-004-0254-x.

[3] GAO Shuo, KONG Teng, ZHANG Man, CHEN Xiao, SUI Yan-wei, REN Yao-jian, QI Ji-qiu, WEI Fu-xiang, HE Ye-zeng, MENG Qing-kun, SUN Zhi. Effects of titanium addition on microstructure and mechanical properties of $CrFeNiTi_x$ (x=0.2−0.6) compositionally complex alloys [J]. Journal of Materials Research, 2019, 34(5): 819−828. https://doi.org/10.1557/jmr.2019.40.

[4] GAO Shuo, CHEN Xiao, SUI Yan-wei, QI Ji-qiu, HE Ye-zeng, WEI Fu-xiang, MENG Qing-kun, SUN Zhi. Corrosion behaviour of $Al_{1.3}CrFeNi$ chemically complex alloy [J]. Canadian Metallurgical Quarterly, 2019, 58(3): 346−355. https://doi.org/10.1080/00084433.2018.1560661.

[5] XIA S Q, YANG X, YANG T F, LIU S, ZHANG Y. Irradiation resistance in $Al_{(x)}CoCrFeNi$ high entropy alloys [J]. JOM, 2015, 67(10): 2340−2344. https://doi.org/10.1007/s11837-015-1568-4.

[6] JUMAEV E, HONG S H, KIM J T, PARK H J, KIM Y S, MUN S C, PARK J Y, SONG G, LEE J K, MIN B H, LEE T, KIM K B. Chemical evolution-induced strengthening on AlCoCrNi dual-phase high-entropy alloy with high specific strength [J]. Journal of Alloys and Compounds, 2019, 777: 828−834. https://doi.org/10.1016/j.jallcom.2018.11.057.

[7] CAO Yuan-kui, LIU Yong, LIU Bin, ZHANG Wei-dong, WANG Jia-wen, DU Meng. Effects of Al and Mo on high temperature oxidation behavior of refractory high entropy alloys [J]. Transactions of Nonferrous Metals Society of China, 2019, 29(7): 1476−1483. https://doi.org/10.1016/S1003-6326(19)65054-5.

[8] SUI Yan-wei, GAO Shuo, CHEN Xiao, QI Ji-qiu, YANG Fei, WEI Fu-xiang, HE Ye-zeng, MENG Qing-kun, SUN Zhi. Microstructures and electrothermal properties of $Al_xCrFeNi$ multi-component alloys [J]. Vacuum, 2017, 144: 80−85. https://doi.org/10.1016/j.vacuum.2017.07.026.

[9] LU Yi-ping, DONG Yong, GUO Sheng, JIANG Li, KANG Hui-jun, WANG Tong-min, WEN Bin, WANG Zhi-jun, JIE Jin-chuan, CAO Zhi-qiang, RUAN Hai-hui, LI Ting-ju. A promising new class of high-temperature alloys: Eutectic high-entropy alloys [J]. Scientific Reports, 2014, 4: 1−5. https://doi.org/10.1038/srep06200.

[10] WANI I S, BHATTACHARJEE T, SHEIKH S, LU Y P, CHATTERJEE S, BHATTACHARJEE P P, GUO S, TSUJI N. Ultrafine-grained $AlCoCrFeNi_{2.1}$ eutectic high-entropy alloy [J]. Materials Research Letters, 2016, 4(3): 174−179. https://doi.org/10.1080/21663831.2016.1160451.

[11] GUO Sheng, NG Chun, LIU C T. Anomalous solidification microstructures in Co-free $Al_xCrCuFeNi_2$ high-entropy alloys [J]. Journal of Alloys and Compounds, 2013, 557: 77−81. https://doi.org/10.1016/j.jallcom.2013.01.007.

[12] HE Feng, WANG Zhi-jun, CHENG Peng, WANG Qiang, LI Jun-jie, DANG Ying-ying, WANG Jin-cheng, LIU C T. Designing eutectic high entropy alloys of $CoCrFeNiNb_x$ [J]. Journal of Alloys and Compounds, 2016, 656: 284−289. https://doi.org/10.1016/j.jallcom.2015.09.153.

[13] CHEN Xiao, QI Ji-qiu, SUI Yan-wei, HE Ye-zeng, WEI Fu-xiang, MENG Qing-kun, SUN Zhi. Effects of aluminum on microstructure and compressive properties of Al−Cr−Fe−Ni eutectic multi-component alloys [J]. Materials Science and Engineering A, 2017, 681: 25−31. https://doi.org/10.1016/j.msea.2016.11.019.

[14] KIM M J, KANG G C, HONG S H, PARK H J, MUN S C, SONG G, KIM K B. Understanding microstructure and mechanical properties of $(AlTa_{0.76})_xCoCrFeNi_{2.1}$ eutectic high entropy alloys via thermo-physical parameters [J]. Journal of Materials Science & Technology, 2020, 57: 131−137. https://doi.org/10.1016/j.jmst.2020.03.045.

[15] YANG Cheng-bo, ZHANG Jing, LI Meng, LIU Xue-jian. Soft-magnetic high-entropy AlCoFeMnNi alloys with dual-phase microstructures induced by annealing [J]. Acta Metallurgica Sinica (English Letters), 2020, 33(8): 1124−1134. https://doi.org/10.1007/s40195-020-01086-0.

[16] REN Ming-xing, LI Bang-sheng, FU Heng-zhi. Formation condition of solid solution type high-entropy alloy [J]. Transactions of Nonferrous Metals Society of China, 2013, 23(4): 991−995. https://doi.org/10.1016/S1003-6326(13)62557-1.

[17] ZHOU Shang-cheng, ZHANG Peng, XUE Yun-fei, WANG Fu-chi, WANG Lu, CAO Tang-qing, TAN Zhen, CHENG Bao-yuan, WANG Ben-peng. Microstructure evolution of $Al_{0.6}CoCrFeNi$ high entropy alloy powder prepared by high pressure gas atomization [J]. Transactions of Nonferrous Metals Society of China, 2018, 28(5): 939−945. https://doi.org/10.1016/S1003-6326(18)64728-4.

[18] WANG Jian-ying, FANG Jing-hua, YANG Hai-lin, LIU Zhi-lin, LI Rui-di, JI Shou-xun, WANG Yun, RUAN Jian-ming. Mechanical properties and wear resistance of medium entropy $Fe_{40}Mn_{40}Cr_{10}Co_{10}/TiC$ composites [J]. Transactions of Nonferrous Metals Society of China, 2019, 29(7): 1484−1494. https://doi.org/10.1016/S1003-6326(19)65055-7.

[19] PENG Jian, LI Zi-yong, JI Xin-bo, SUN Yan-le, FU Li-ming, SHAN Ai-dang. Decomposition kinetics of carbon-doped FeCoCrNiMn high-entropy alloy at intermediate temperature [J]. Transactions of Nonferrous Metals Society of China, 2020, 30(7): 1884−1894. https://doi.org/10.1016/S1003-6326(20)65347-X.

[20] LI C, LI J C, ZHAO M, ZHANG L, JIANG Q. Microstructure and properties of $AlTiNiMnB_x$ high entropy alloys [J]. Materials Science and Technology, 2008, 24(3): 376−378. https://doi.org/10.1179/174328408X275964.

[21] LEE C P, CHEN Y Y, HSU C Y, YEH J W, SHIH H C. The effect of boron on the corrosion resistance of the high entropy alloys $Al_{0.5}CoCrCuFeNiB_x$ [J]. Journal of the Electrochemical Society, 2007, 154(8): C424−C430. https://doi.org/10.1149/1.2744133.

[22] SHAYSULTANOV D G, SALISHCHEV G A, IVANISENKO Y V, ZHEREBTSOV S V, TIKHONOVSKY M A, STEPANOV N D. Novel $Fe_{36}Mn_{21}Cr_{18}Ni_{15}Al_{10}$ high entropy alloy with bcc/B2 dual-phase structure [J]. Journal of Alloys and Compounds, 2017, 705: 756−763. https://doi.org/z10.1016/j.jallcom.2017.02.211.

[23] LIU Xiao-tao, LEI Wen-bin, MA Li-juan, LIU Jin-ling, LIU Jing, CUI Jian-zhong. Effect of boron on the microstructure, phase assemblage and wear properties of $Al_{0.5}CoCrCuFeNi$ high-entropy alloy [J]. Rare Metal Materials and Engineering, 2016, 45(9): 2201−2207. https://doi.org/10.1016/S1875-5372(17)30003-6.

[24] SIEGRIST T, JOST P, VOLKER H, WODA M, MERKELBACH P, SCHLOCKERMANN C, WUTTIG M. Disorder-induced localization in crystalline phase-change materials [J]. Nature Materials, 2011, 10(3): 202−208. https://doi.org/10.1038/nmat2934.

[25] LI Pan-pan, WANG An-ding, LIU C T. Composition dependence of structure, physical and mechanical properties of $FeCoNi(MnAl)_{(x)}$ high entropy alloys [J]. Intermetallics, 2017, 87: 21−26. https://doi.org/10.1016/j.intermet.2017.04.007.

[26] JIANG Hui, QIAO Dong-xu, JIAO Wen-na, HAN Kai-ming, LU Yi-ping, LIAW P K. Tensile deformation behavior and mechanical properties of a bulk cast $Al_{0.9}CoFeNi_2$ eutectic high-entropy alloy [J]. Journal of Materials Science & Technology, 2021, 61: 119−124. https://doi.org/10.1016/j.jmst.2020.05.053.

[27] CHEN Qiu-shi, LU Yi-ping, DONG Yong, WANG Tong-min, LI Ting-ju. Effect of minor B addition on microstructure and properties of AlCoCrFeNi multi-compenent alloy [J]. Transactions of Nonferrous Metals Society of China, 2015, 25(9): 2958−2964. https://doi.org/10.1016/S1003-6326(15)63922-X.

添加微量 B 元素对 $Al_{19}Co_{20}Fe_{20}Ni_{41}$ 共晶高熵合金显微组织及性能的影响

冯俊杰[1]，高 硕[1]，韩 昆[1]，苗屹冬[1]，戚继球[1]，

委福祥[1]，任耀剑[1]，占珍珍[1]，隋艳伟[1]，孙 智[1]，曹 鹏[2]

1. 中国矿业大学 材料与物理学院 江苏省高效储能技术与装备工程实验室，徐州 221116；
2. Department of Chemical and Materials Engineering, The University of Auckland, Private Bag 92019, Auckland, 1142, New Zealand

摘 要：同时强化合金的力学性能和磁性能是软磁材料的理想化制备策略。通过制备非等原子比的 $Al_{19}Co_{20}Fe_{20}Ni_{41}$ 共晶高熵合金，研究硼元素合金化对显微组织演变、相形成、力学性能和软磁性能的影响。随着 B 含量的增加，$(Al_{19}Co_{20}Fe_{20}Ni_{41})_{100-x}B_x$ 合金的显微组织从最初的层片状共晶组织(x=0)转变为离异共晶组织(x>0.6)。细小的硼化物从晶间相中析出(x≥0.6)。合金的硬度从 HV 328.66 增加到 HV 436.34。压缩力学性能测试结果显示合金发生从塑性材料向脆性材料的转变。$Al_{19}Co_{20}Fe_{20}Ni_{41}$ 合金具有良好的软磁性能，微量的 B 添加对其软磁性能的影响很微弱。当用作软磁性材料时，合金电阻率的增加可以有效地减少涡流损耗。

关键词：高熵合金；硼元素；显微组织；力学性能；软磁特性

(Edited by Xiang-qun LI)